DOI: 10.1002/chem.200902902

Homoleptic Tris(Pyridyl Pyrazolate) Ir^{III} Complexes: En Route to Highly Efficient Phosphorescent OLEDs

Kellen Chen,[a] Cheng-Han Yang,[a] Yun Chi,*[a] Chao-Shiuan Liu,[a] Chih-Hao Chang,[b] Chung-Chia Chen,[b] Chung-Chih Wu,*[b] Min-Wen Chung,[c] Yi-Ming Cheng,[c] Gene-Hsiang Lee,[c] and Pi-Tai Chou*[c]

Abstract: Treatment of the metal reagent $IrCl_3{\cdot}nH_2O$ with two equivalents of 2-pyridyl pyrazole (N^N)H (3-*tert*-butyl-5-(2-pyridyl) pyrazole, (bppz)H and 3-trifluoromethyl-5-(2-pyridyl) pyrazole, (fppz)H), afforded the isomeric Ir^{III} metal complexes with a general formula *cis*-$[Ir(bppz)_2Cl_2]H$ (**2a**), *trans*-$[Ir(bppz)_2Cl_2]H$ (**3a**), *cis*-$[Ir(fppz)_2Cl_2]H$ (**2b**), and *trans*-$[Ir(fppz)_2Cl_2]H$ (**3b**). Single-crystal X-ray diffraction studies on **2b** and **3a** revealed the coexistence of two pyrazolate chelates and two terminal chloride ligands on the coordination sphere. Subsequent reactivity studies confirmed their intermediacy to the preparation of homoleptic *mer*-$[Ir(bppz)_3]$ (**1a**) and *mer*-$[Ir(fppz)_3]$ (**1b**) that showed dual intraligand and ligand-to-ligand charge-transfer phosphorescence at room temperature. To attain bright, room-temperature phosphorescence further, we then synthesized two isoquinolinyl pyrazolate complexes, *mer*-$[Ir(bipz)_3]$ (**4a**) and *mer*-$[Ir(fipz)_3]$ (**4b**) ((bipz)H = 3-*tert*-butyl-5-(1-isoquinolyl) pyrazole and (fipz)H = 3-trifluoromethyl-5-(1-isoquinolyl) pyrazole). Their orange luminescence is mainly attributed to the mixed MLCT/ππ* transition, and the quantum yields were as high as 86 (**4a**) and 50% (**4b**) in degassed CH_2Cl_2 solution at RT. The organic light-emitting diodes (OLEDs) were then fabricated by using **4a** as a dopant, giving orange luminescence with $CIE_{x,y} = 0.55$, 0.45 ($CIE_{x,y}$ = the 1931 Commission Internationale de L'Eclairage (x,y) coordinates) and peak efficiencies of 14.6% photon/electron, 34.8 cd A^{-1}, 26.1 lm W^{-1}. The device data were then compared with the previously reported heteroleptic complex $[Ir(dfpz)_2(bipz)]$ (**5**) ((dfpz)H = 1-(2,4-difluorophenyl) pyrazole), revealing the possible effect of the bipz chelate and phosphor design on the overall electrophosphorescent performance, which can be understood by the differences in the carrier-transport properties.

Keywords: density functional calculations · iridium · luminescence · N ligands · phosphorescence

Introduction

Iridium(III)-based phosphorescent complexes have received considerable attention owing to their latent applications in organic light-emitting diodes (OLEDs).[1] It is well understood that their photophysical properties are strongly dependent on the character of their frontier orbitals and the resulting HOMO/LUMO energy gap, which in turn are governed by their basic skeletal arrangement and the electronic properties of substituents anchored to these chelating chromophores. Tuning of emission wavelengths over the entire visible spectra was successfully achieved by ingenious modification of their ligating chromophores that included both the chromophoric and/or ancillary ligands.[2] Both saturated-red and true-blue phosphors were isolated and shown to be good candidates for phosphorescent OLED fabrications. The majority of complexes that fit into this category are called heteroleptic complexes, showing the existence of two

[a] K. Chen, Dr. C.-H. Yang, Prof. Y. Chi, Prof. C.-S. Liu
Department of Chemistry, National Tsing Hua University
Hsinchu 300 (Taiwan)
Fax: (+886) 3-572-0864
E-mail: ychi@mx.nthu.edu.tw

[b] C.-H. Chang, C.-C. Chen, Prof. C.-C. Wu
Department of Electrical Engineering
Graduate Institute of Photonics and Optoelectronics and
Graduate Institute of Electronics Engineering
National Taiwan University, Taipei 106 (Taiwan)
Fax: (+886) 2-2367-1909
E-mail: chungwu@cc.ee.ntu.edu.tw

[c] M.-W. Chung, Dr. Y.-M. Cheng, Dr. G.-H. Lee, Prof. P.-T. Chou
Department of Chemistry, National Taiwan University
Taipei 106 (Taiwan)
Fax: (+886) 2-2369-5208
E-mail: chop@ntu.edu.tw

Supporting information for this article is available on the WWW under http://dx.doi.org/10.1002/chem.200902902.

cyclometalated chelates plus one ancillary ligand with a greater ligand-centered ππ* energy gap, such that its interference to the photoexcitation, relaxation, and consequent luminescence can be minimized. On the other hand, reports on the highly emissive homoleptic Ir^{III} complexes with all cyclometalated chelates are still rare.[3] An obstacle lies in the higher temperatures required for their syntheses, because the majority of cyclometalated chelates cannot withstand such stringent reaction conditions, leading to severe decomposition.[4] In sharp contrast, noncyclometalated homoleptic complexes such as trisubstituted acetylacetonate $[Ir(acac)_3]$,[5] quinolinolate $[Ir(Q)_3]$,[6] and even picolinate complexes $[Ir(pic)_3]$ are known;[7] unfortunately, none of them exhibit respectable room-temperature phosphorescence in both fluid and solid states.

Following this research direction, we have examined the reactions of $IrCl_3{\cdot}nH_2O$ with 3-*tert*-butyl-5-(2-pyridyl) pyrazole ((bppz)H) and with 3-trifluoromethyl-5-(2-pyridyl) pyrazole ((fppz)H) in anticipation of isolating the respective homoleptic complexes *mer*-$[Ir(bppz)_3]$ (**1a**) and $[Ir(fppz)_3]$ (**1b**).[8] Although these Ir^{III} complexes failed to exhibit the anticipated bright phosphorescence at room temperature, we serendipitously observed a unique case of dual emission, of which the intensity ratio and the associated relaxation dynamics of each peak show remarkable temperature dependence. This result highlights an unusual intraligand charge-transfer (ILCT) to ligand-to-ligand charge-transfer (LLCT) conversion, that is, an electron-transfer-like excited-state process (see below) for which the LLCT has not only lowered the emission efficiency but also resulted in an unwanted bathochromatic shift.[8]

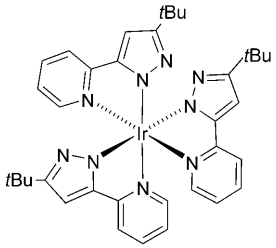

mer-$[Ir(bppz)_3]$ (**1a**)

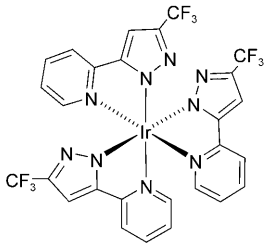

mer-$[Ir(fppz)_3]$ (**1b**)

Herein, we report the mechanistic details that gave the formation of both **1a** and **1b**, which is highlighted by the isolation of two reaction intermediates (*cis*-**2a** and *cis*-**2b** and *trans*-**3a** and *trans*-**3b**) upon treatment of $IrCl_3{\cdot}nH_2O$ with only two equivalents of (bppz)H and (fppz)H chelates. Their role in the transformation is also established.

We have extended the scope of these investigations by employing other chelating azolate ligands (3-*tert*-butyl-5-(1-isoquinolyl) pyrazole, (bipz)H and 3-trifluoromethyl-5-(1-isoquinolyl) pyrazole, (fipz)H), and have obtained the related trisubstituted *mer*-$[Ir(bipz)_3]$ (**4a**) and $[Ir(fipz)_3]$ (**4b**). Remarkably, both complexes showed bright-orange phosphorescence at RT, giving the opportunity to examine their

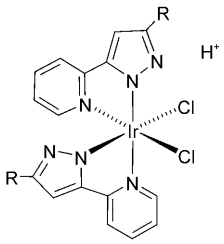

(**2a**), R = *t*Bu
(**2b**), R = CF_3

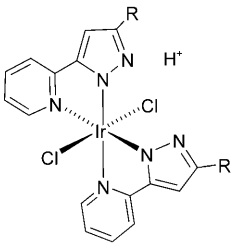

(**3a**), R = *t*Bu
(**3b**), R = CF_3

latent applications as OLED dopants. For complex **4a**, the performance data were compared with a previously reported heteroleptic Ir^{III} complex with a single isoquniolinyl azolate ligand, $[Ir(dfpz)_2(bipz)]$ (**5**).[9] This comparison provides a case in point to evaluate the effect of emitting chromophoric chelates. Therefore, the data accumulated in this study allow us to gain more insight into the photophysical and device behavior between two closely related molecular designs.

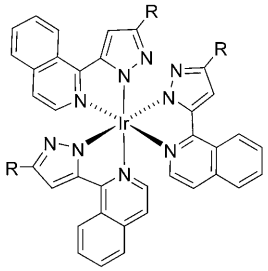

mer-$[Ir(bipz)_3]$ (**4a**), R = *t*Bu
mer-$[Ir(fipz)_3]$ (**4b**), R = CF_3

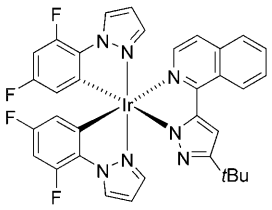

$[(dfpz)_2Ir(bipz)]$ (**5**)

Results and Discussion

Synthesis and characterization: It has been reported that $IrCl_3{\cdot}nH_2O$ reacts with two equivalents of cyclometalated ligands, for example (C^N)H, in 2-ethoxyethanol at reflux under fairly mild conditions to give excellent yields of the chloride-bridged dimer, $[(C^N)_2Ir(\mu\text{-}Cl)]_2$ (Scheme 1). Crystallographic studies show that each octahedral Ir^{III} metal center of the dimer is coordinated by the two bridging chlorides and two C^N chelates for which the neutral N donor is located at the *trans* disposition.[10] The respective tricyclometalated complexes $[Ir(C^N)_3]$ were then obtained upon treatment of this chloride-bridged dimer with more cyclometalated ligand at a higher temperature.[11] In yet another approach, $[Ir(C^N)_3]$ can also be obtained by simply combining the iridium reagents, for example, $[Ir(acac)_3]$ or $IrCl_3{\cdot}nH_2O$, with an excess of C^N ligands at significantly higher temperatures or in presence of a chloride scavenger.[12]

Recent reports indicated that both the cyclometalated ligand (C^N)H and pyridyl azole ligand (N^N)H are capa-

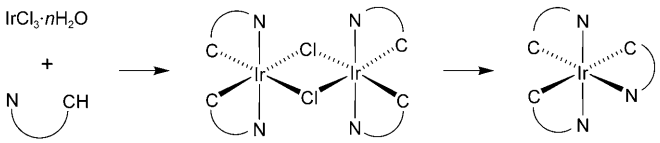

Scheme 1.

ble of reacting with reagents $M_3(CO)_{12}$, M = Ru and Os, to afford good yields of octahedral complexes $[M(C^N)_2(CO)_2]$ and $[M(N^N)_2(CO)_2]$, respectively.[13,14] This implies that the (N^N)H ligand could react with $IrCl_3{\cdot}nH_2O$ to afford trisubstituted $[Ir(N^N)_3]$ in a fashion akin to the previously mentioned, meridional $[Ir(C^N)_3]$ cyclometalates.

Indeed, treatment of excessive (N^N)H with $IrCl_3{\cdot}nH_2O$ afforded the meridional $[Ir(C^N)_3]$ derivatives **1a** and **b** and **4a** and **b** in high yields, confirming the cyclometalating behavior of these chelates. The intermediates **2a** and **b** and **3a** and **b** with the general formula $[Ir(N^N)_2Cl_2]H$ were also obtained from treatment of $IrCl_3{\cdot}nH_2O$ with two equivalents of pyridyl pyrazoles (bppz)H and (fppz)H in methoxyethanol at reflux, for which the implied mechanism is somewhat identical to that of the dimer $[(C^N)_2Ir(\mu\text{-}Cl)]_2$ isolated from the reactions with the cyclometalating ligands.[12] Moreover, these complexes were easily separated by silica-gel column chromatography. These intermediates are stable and soluble in typical organic solvents, but are barely emissive under all conditions, even at 77 K. The ^{1}H NMR spectral patterns of **2a** and **3a** (or **2b** and **3b**) are consistent with the existence of nonequivalent and equivalent pyrazolate chelates, respectively. Thus, five aromatic proton resonances corresponding to the pyrazolate chelates were resolved for the *trans*-chloride complexes **3a** and **3b**, whereas a more complicated spectral pattern was detected for *cis*-complexes **2a** and **2b** that showed asymmetric arranged pyrazolate chelates and *cis*-Cl,Cl disposition. In contrast to the Pt^{II} complexes with identical neutral pyrazole chelate,[15] the N–H proton of these Ir^{III} complexes cannot be unambiguously defined in their ^{1}H NMR spectra owing to the enhanced and reversible dissociation of the proton, even in non-polar solvent such as $CDCl_3$ or $[D_8]$toluene.

Moreover, the intermediacy of **2** and **3** versus the formation of trisubstituted **1** was demonstrated by conducting further chelate substitution at higher temperatures. In fact, our control reaction has revealed the occurrence of a slow interconversion between *cis* and *trans* isomers at the elevated temperature. Moreover, treatment of either the *cis* or *trans* complexes **2a**, **3a** and **2b**, **3b** had afforded a reasonable amount of the anticipated Ir^{III} complexes **1a** and **1b**, confirming the previous observation.[8] However, for executing scale-up preparation, it is best to bypass the isolation of **2** and **3** and employ at least three equivalents of pyrazole in a higher-boiling-point solvent such as diethylene glycol monoethyl ether (DGME). Similarly, the related isoquinolinyl derivatives **4a** and **4b** were obtained in good yields, without the prior isolation of respective dichloride intermediates.

X-ray crystallography: To investigate their molecular structures further, we carried out single-crystal X-ray analyses on both **2a** and **3b**; their ORTEP diagrams are given in Figure 1 and Figure 2, respectively. As expected, complex **2a** exhibited the orthogonal arrangement of bppz chelates, with the average Ir–N(pyridyl) lengths being slightly longer than that of the Ir–N(pyrazolate) lengths, which is typical for such pyridyl pyrazolate chelates.[16] However, owing to the poor accuracy of the crystallographical parameters, we unfortunately are unable to locate the hydrogen atom (or

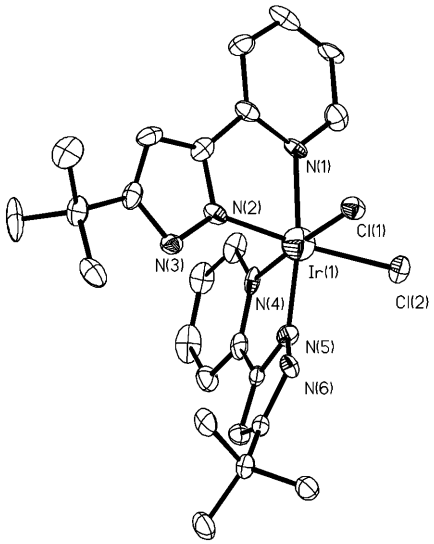

Figure 1. ORTEP diagram of **2a** with thermal ellipsoids shown at the 50% probability level. Selected bond lengths [Å]: Ir–N(1) = 2.073(7), Ir–N(2) = 1.993(8), Ir–N(4) = 2.024(8), Ir–N(5) = 1.991(8), Ir–Cl(1) = 2.356(2), and Ir–Cl(2) = 2.373(2).

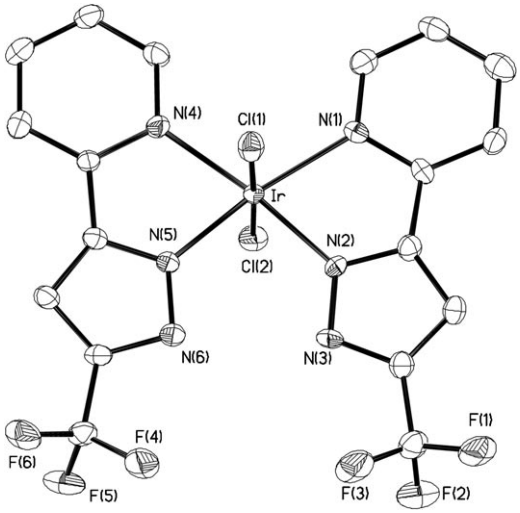

Figure 2. ORTEP diagram of **3b** with thermal ellipsoids shown at the 50% probability level. Selected bond lengths [Å]: Ir–N(1) = 2.124(5), Ir–N(2) = 1.978(5), Ir–N(4) = 2.087(5), Ir–N(5) = 1.968(5), Ir–Cl(1) = 2.351(1), and Ir–Cl(2) = 2.333(1).

proton) that is essential to balance the formal negative charge associated with the Ir^{III} fragment. One possibility is to assign this proton on the water molecule present in the asymmetric unit. If this were the case, complex **2a** can be considered as an anionic fragment with the tentative formula *cis*-$[Ir(bppz)_2Cl_2]^-$.

In the case of **3b**, however, the chlorides adopt a *trans*-disposition with the pyrazolate chelates residing on the four corners of the equatorial plane. Note that both pyridyl groups of fppz chelates are now arranged in a *cis* fashion to one another. Such a geometrical feature is in sharp contrast with that observed in the related octahedral Os^{II} complexes, in which the pyrazolate chelates showed distinctive *trans* orientation along with the formation of a pair of C–H···N inter-ligand hydrogen bonding.[17] This unusual structural arrangement gives a hint to the position of unidentified proton in **3b** that lies in between the N(3) and N(6) atoms of the pyrazolate fragments. Again, the location of this hydrogen atom cannot be unambiguously defined.

Figure 3 gives the ORTEP diagram of the trisubstituted isoquinolinyl complex **4a**, showing the meridional arrangement of bipz ligands that is attributed to the reduction of steric repulsion among *tert*-butyl substituents, whereas the facial isomer would have all three *tert*-butyl groups pointing towards the identical triangular face of octahedral coordination geometry and cause excessive spatial congestion. Moreover, the Ir–N bond lengths for isoquinolinyl (≈2.073–2.040 Å) and pyrazolate fragments (≈2.027 and 2.010 Å) are reminiscent of those observed in previously reported **1a**, but are shorter than those (≈2.16 and ≈2.11 Å) of the related heteroleptic $[Ir(C^N)_2(N^N)]$, for which the unique pyridyl azolate N^N chelate resides opposite the carbon atom of both cyclometalated chromophores.[18] Note that the N(8) atom of **4a** shows the shortest Ir–N bond length of 2.010(6) Å, which is due to the increased interaction at this pyrazolate site and less competition (in view of the bonding) from its *trans*-isoquinolinyl group, and the latter shows the longest Ir–N(1) length of 2.073(5) Å of all Ir–N interactions.

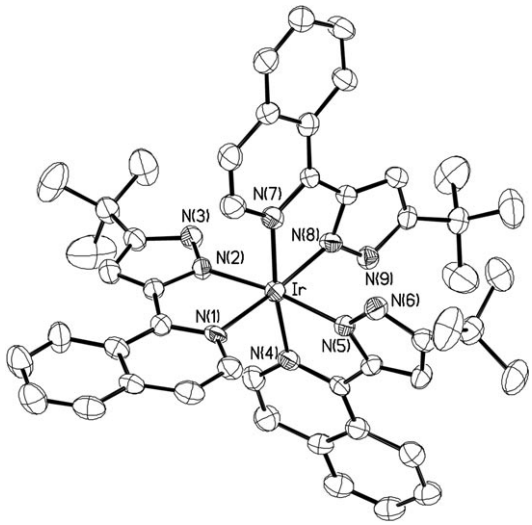

Figure 3. ORTEP diagram of complex **4a** with thermal ellipsoids shown at the 30% probability level. Selected bond lengths [Å]: Ir–N(1) = 2.073(5), Ir–N(2) = 2.027(5), Ir–N(4) = 2.040(4), Ir–N(5) = 2.025(6), Ir–N(7) = 2.049(6), and Ir–N(8) = 2.010(6).

Photophysical data: The absorption and emission spectra of **4a** and **4b** are displayed in Figure 4 and the data are summarized in Table 1. Both complexes exhibit well-resolved

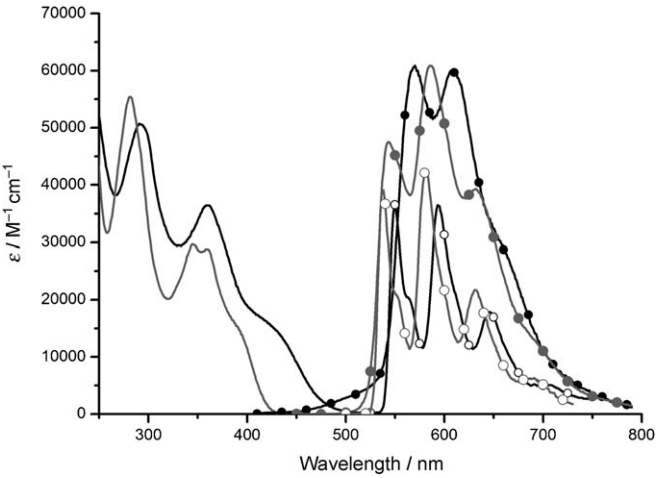

Figure 4. Absorption and luminescence spectra of **4a** (black) and **4b** (grey) in CH_2Cl_2 under degassed conditions at room temperature (●) and at 77 K (○).

ππ* transitions ≤365 nm ($\varepsilon \geq 3\times10^4\,M^{-1}cm^{-1}$), whereas the lower-energy shoulder around 430 and 400 nm ($\varepsilon \approx 10^4\,M^{-1}cm^{-1}$) is reasonably attributed to the tailing of ππ* transitions that are mixed, to a certain extent, with metal-to-ligand charge transfer (MLCT) transitions. The whole assignment is well supported by the well-matched absorption spectral patterns versus those of **1a** and **1b** (see Figure 5),[8] except that all peaks appear at relatively longer wavelengths, due to the greater π conjugation of the isoquinolinyl than that of the pyridyl moieties.

Table 1. Photophysical properties for complexes **1a**, **1b**, **4a**, **4b**, and **5** in CH_2Cl_2 solution.

Complex	Absorption λ_{max} [nm] ($\varepsilon\times10^{-3}$ [$M^{-1}cm^{-1}$])	λ_{em} [nm], RT	λ_{em} [nm], 77 K[a]	Φ	τ [μs]
1a[b]	271 (34.0), 323 (24.2), 378 (6.4)	565, 531	445, 474, 500	0.0008	7.1
1b[b]	260 (39.0), 306 (24.6), 355 (6.2)	528, 523	427, 454, 479	0.0067	6.3
4a	291 (50.8), 360 (36.3), 420 (15.9)	567, 603 (636)	549, 593, 646	0.86	11.2
4b	281 (55.3), 345 (29.8), 360 (29.1), 386 (16.4)	544, 586, 631	537, 582, 621	0.49	40.7
5[c]	252 (24.1), 302 (14.6), 358 (6.4), 416 (3.3)	562, 596	–	1.0	20.2

[a] The emission properties were resolved in an CH_2Cl_2 matrix at 77 K. [b] See Ref. [8]. [c] See Ref. [9].

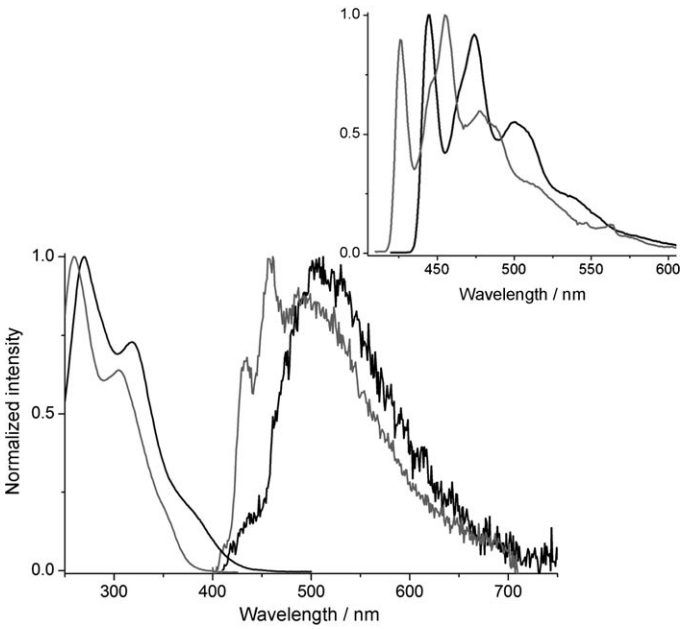

Figure 5. Absorption and luminescence spectra of **1a** (black) and **1b** (gray) in CH_2Cl_2 under degassed conditions at room temperature. Inset: Luminescence spectra of **1a** and **1b** in CH_2Cl_2 at 77 K.

As for the emission spectra, unlike the rather weak, dual phosphorescence of **1a** and **1b** observed in degassed CH_2Cl_2 solution at room temperature,[8] complexes **4a** and **4b** all show unique, bright luminescence (e.g., $\Phi_{4a} \approx 0.86$ and $\Phi_{4b} \approx 0.50$) consisting of a notable vibronic progression (500–800 nm) with the first peak appearing at 567 and 545 nm, respectively (see Figure 4). The poor overlap between the emission signals and the lowest-energy absorption band for both **4a** and **4b** can be attributed to the origin of emission possessing excessive ligand-centered $\pi\pi^*$ and relatively low MLCT character. It has been well established that the metal d_π orbital is directly coupled into the spin-orbit-coupling matrix. Thus, low MLCT percentage causes poor mixing between singlet and triplet manifolds, resulting in a relatively large separation between the absorption (S_0–S_1) and emission band (T_1–S_0). The great increase of the $\pi\pi^*$ property for the lowest-lying transition also leads to the appearance of a vibronic emission profile that is consistent with the experimental observation. Upon lowering the temperature to 77 K, both **4a** and **4b** show similar emission spectral profiles with respect to those acquired at room temperature, except for a slightly hypsochromic shift, for example, a shift of λ_{em} from 567–549 nm (from RT–77 K) for **4a** and from 544–537 nm (from RT–77 K) for **4b**. This phenomenon is tentatively ascribed to occur as a consequence of the lack of solvent reorientation invoked by the formation of a solid-state solvent matrix at 77 K, resulting in a destabilization of energy in the excited state. The differences between **4a** and **4b** in view of the lowest-lying absorption and likewise the emission peak wavelengths can be mainly attributed to the *tert*-butyl (**4a**) versus trifluoromethyl (**4b**) substitution in which the *tert*-butyl substituent in **4a** elevates the pyrazolate (HOMO) orbital energy, resulting in the reduction of the energy gap. Conversely, enlargement of the energy gap is expected for **4b** owing to the electron-withdrawing trifluoromethyl substituent that effects the HOMO of the pyrazolate moiety. Firm support of this viewpoint is provided by the computational approaches described below.

Time-dependent DFT calculations (performed by using functional PBE0 associated with the basis set 6-31G(d)/LANL2DZ, see the Experimental Section for details) was then performed to gain more insight into the fundamental basis. Figure 6 and Figure 7 depict the selected molecular orbitals involved in the lower-lying transitions of complexes **4a** and **4b**, respectively. The rest of the frontier orbitals are provided in Figures S1 and S2 in the Supporting Information. All pertinent energy gaps and corresponding assignments of each transition are listed in Table 2 (**4a**) and Table 3 (**4b**). The calculated energy gaps of the $S_0 \rightarrow S_1$ tran-

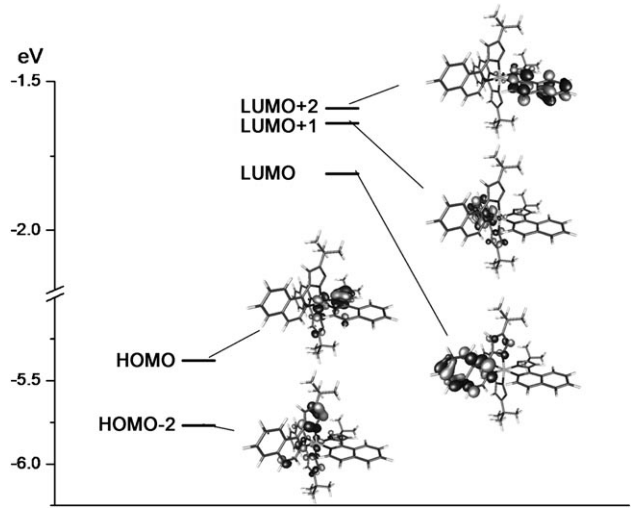

Figure 6. Selected molecular orbitals involved in the lower-lying electronic transitions of **4a**.

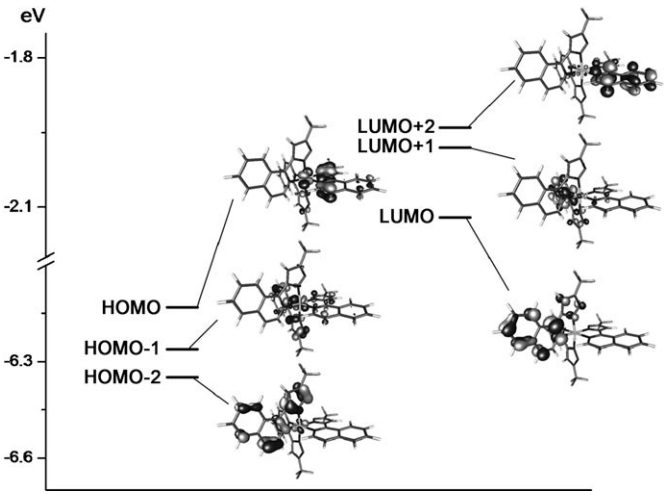

Figure 7. Selected molecular orbitals involved in the lower-lying electronic transitions of **4b**.

Table 2. The calculated wavelength (λ), oscillator strength (f) and orbital transition analyses of **4a**.

Main transition	State	λ_{cal}	f	Assignment	MLCT [%]
LLCT	S_1	445	0.03	HOMO→LUMO (94%) HOMO→LUMO+2 (47%) HOMO−1→LUMO+2 (36%)	18.71
ILCT	T_1	558.4	0	HOMO−3→LUMO+2 (11%) HOMO−2→LUMO+2 (7%) HOMO−7→LUMO+2 (7%) HOMO−2→LUMO (56%) HOMO−1→LUMO (24%)	13.17
ILCT	T_2	553	0	HOMO−4→LUMO (16%) HOMO−10→LUMO (5%) HOMO−3→LUMO (5%) HOMO−2→LUMO+1 (31%) HOMO−3→LUMO+1 (26%)	8.84
ILCT	T_3	546.1	0	HOMO−1→LUMO+1 (22%) HOMO→LUMO+1 (20%) HOMO−8→LUMO+1 (6%) HOMO→LUMO (32%) HOMO→LUMO+2 (20%)	8.52
LLCT	T_4	451	0	HOMO−3→LUMO+2 (13%) HOMO−1→LUMO+2 (10%) HOMO−5→LUMO+2 (5%) HOMO→LUMO+1 (38%) HOMO−3→LUMO+1 (13%)	11.96
LLCT	T_5	441.4	0	HOMO→LUMO+2 (13%) HOMO→LUMO (8%) HOMO−5→LUMO+1 (8%) HOMO→LUMO (20%)	11.94
LLCT	T_6	433.8	0	HOMO−1→LUMO (16%) HOMO→LUMO+2 (14%) HOMO→LUMO+1 (8%)	13.96

Table 3. The calculated wavelength (λ), oscillator strength (f) and orbital transition analyses of **4b**.

Main transition	State	λ_{cal}	f	Assignment	MLCT [%]
LLCT	S_1	383	0.02	HOMO→LUMO (88%) HOMO−2→LUMO (89%)	15.00
ILCT	T_1	532.4	0	HOMO−4→LUMO (7%) HOMO−2→LUMO+1 (6%) HOMO−9→LUMO+6 (5%) HOMO→LUMO+2 (59%)	6.93
ILCT	T_2	531.6	0	HOMO−1→LUMO+2 (26%) HOMO−3→LUMO+2 (10%) HOMO→LUMO+1 (8%) HOMO−1→LUMO+1 (51%) HOMO−3→LUMO+1 (19%)	12.91
ILCT	T_3	528.2	0	HOMO−1→LUMO (9%) HOMO−2→LUMO+1 (9%) HOMO→LUMO+1 (8%) HOMO−1→LUMO+2 (5%) HOMO→LUMO+1 (19%) HOMO→LUMO (16%)	9.45
LLCT	T_4	391.7	0	HOMO−3→LUMO+1(15%) HOMO−3→LUMO+2 (9%) HOMO→LUMO+2 (9%) HOMO−1→LUMO+2 (7%) HOMO→LUMO (40%)	11.63
LLCT	T_5	388.2	0	HOMO−4→LUMO (21%) HOMO→LUMO+2 (12%) HOMO−3→LUMO+2 (8%) HOMO→LUMO+1 (19%) HOMO→LUMO+2 (16%)	16.18
LLCT	T_6	384	0	HOMO−3→LUMO+2 (11%) HOMO−4→LUMO (10%) HOMO−1→LUMO (6%) HOMO−3→LUMO+1 (6%)	11.77

sition for **4a** (445 nm) and **4b** (383 nm) are close to the observed onsets (an appearance of a shoulder in Figure 4) of the absorption spectra recorded in CH_2Cl_2 solution. Moreover, the calculated energy gaps of the T_1 states for **4a** (558 nm) and **4b** (532 nm) are also in agreement with the trend of the first vibronic peak of their emission spectra. This result indicates that the time-dependent DFT (TDDFT) calculation, in a qualitative manner, can predict the lowest Franck–Condon absorption in the singlet manifold as well as the phosphorescence energy gap based on the S_0 geometries of the studied organometallic complexes.

As for the transition characteristics, frontier orbital analyses indicate that **4a** and **4b** show the lowest-lying S_0–T_1 transition composed of ligand $\pi\pi^*$ transfer and, to a lesser extent (<15%), of MLCT. The $\pi\pi^*$ domination indirectly supports the vibronic progression depicted in the phosphorescence spectra. As shown in Tables 2 and 3, the lower-lying triplet manifold for **4a** and **4b** consists of two sets of closely lying transitions, T_1 –T_3 and T_4–T_6, for which the calculated energy difference among T_1–T_3 (or T_4–T_6) are very small (<2 kcal mol^{-1}), which, within theoretical error, may be treated as two sets of triple degenerate states. Detailed frontier orbital analyses also led to the conclusion that the T_1–T_3 and T_4 –T_6 states, in view of $\pi\pi^*$ transitions only, could be assigned to ILCT (within bipz or fipz moiety) and LLCT (pyrazolate→isoquniolinyl moiety), respectively. The energy difference between ILCT and LLCT is calculated to be as large as approximately 12 kcal mol^{-1} and 19 kcal mol^{-1} for **4a** and **4b**, respectively. Compared with **1a** and **1b**, in which T_{ILCT}

and T_{LLCT} are nearly degenerate and rapid interconversion takes place,[8] the much lower energy for T_{ILCT} in **4a** and **4b** can be rationalized by the elongation of π conjugation in the isoquinolinyl pyrazolate moiety, resulting in a smaller ILCT gap.

The strategy of elongation upon π conjugation from pyridine (**1a**, **1b**) to isoquinoline (**4a**, **4b**), as evidenced by the above experimental results, has significant effects on improving the emission properties in, for example, the quantum yield and long-lived emission lifetime.[19] It is generally believed that far separation between metal center d_π–d_{σ^*} transitions (^{3}MC) and the responding emissive state, for example the ^{3}MLCT/ππ* state, plays a key role for the π-elongation effect. Herein, the proof of concept for tuning the energy gap between ^{3}MLCT/ππ* and ^{3}MC states is conducted by using complexes **1b** and **4b**. In this approach, the higher-lying ^{3}MC state was calculated according to the methodology illustrated in the work of Persson et al.[20] Details of the calculation procedures are described in the Experimental Section. The result shown in Figure 8 clearly indicates that the isoquinolinyl pyrazolate ligand of **4b** renders better π conjugation. The net result is to decrease the π* orbital and hence the reduction of the ^{3}MLCT/ππ* energy in **4b**, whereas ^{3}MC is much less affected. This should lead to a larger energy difference between ^{3}MLCT and ^{3}MC dd excited states for **4b** of approximately 0.56 eV (12.9 kcal mol^{-1}), whereas for **1b** the ^{3}MC state is even lower than the ^{3}MLCT/ππ* state by approximately 0.15 eV (3.46 kcal mol^{-1}). However, for **4b** an additional factor that invokes better electron-withdrawing behavior of the isoquinolinyl fragment that stabilizes the d_π orbitals of the Ir^{III} metal center to account for the higher MC state cannot be eliminated. For **1b**, owing to the proximity in energy levels, the ^{3}MLCT/ππ*→^{3}MC→S_0 radiationless pathway is expected to be efficient, accounting for its weak emissive nature

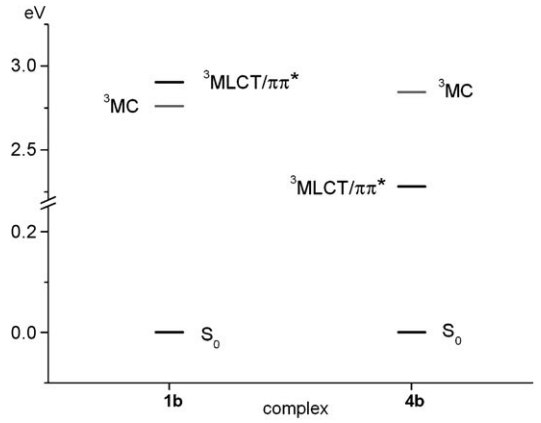

Figure 8. Energy diagram of complexes **1b** and **4b** in terms of ^{3}MC and ^{3}MLCT/ππ* states, in which the ^{3}MLCT/ππ* state denotes the lowest triplet electronic state obtained from unrestricted optimization, starting from X-ray structural results. The ^{3}MC state is also refined by the same method but with a distorted initial geometry. Note that the S_0 level for **1b** and **4b** has been normalized.

(i.e., relatively low quantum yield (0.0067) and short observed lifetime ($\tau_{obs} \approx 6.3$ μs)) compared with that of **4b** (quantum yield (0.49), and $\tau_{obs} \approx 40.7$ μs, see Table 1), and vice versa for **1a** and **4a** (see Table 1). A similar strategy has been successfully applied in the design and synthesis of Ru^{II} complexes showing bright room-temperature phosphorescence.[21]

Finally, as shown in Tables 2 and 3, for both S_1 and T_1 states, the %MLCT in **4a** is calculated to be slightly larger than that in **4b**. This result seems to be contradictory to the *tert*-butyl electron-donating properties, which should elevate the chelate π contribution to the HOMO and hence relatively discount the d_π contribution of the Ir^{III} metal ion in **4a**. The results may be rationalized by an indirect induction effect in which the electron donation is passed by the *tert*-butyl substituent of **4a**. Thus, one can envisage the electron delocalization from the *tert*-butyl-substituted pyrazolate transmitting through the central Ir^{III} metal ion and extending to the isoquinolinyl moiety; the net effect is to enhance the metal–ligand interaction as well as to increase the electron density at the Ir^{III} center and hence to give more MLCT character. Note that increase of %MLCT enhances the spin-orbit coupling and hence results in a larger radiative decay rate constant k_r. This is consistent with the experimental observation, which shows larger k_r for **4a** ($k_r \approx 7.7 \times 10^4$ s^{-1}, compared with **4b** $\approx 1.2 \times 10^4$ s^{-1}).

Electroluminescence properties of OLED devices: With its rather high quantum efficiency, **4a** was then subject to electroluminescent studies. The results were compared with those of the heteroleptic complex **5** based on the same luminescence chromophore.[9] To achieve highly efficient phosphorescent OLEDs (PhOLEDs), several criteria should be satisfied in the architecture design. First, a host with the triplet energy higher than that of the phosphorescent guest is desirable to facilitate the exothermic energy transfer from the host to the guest and to prohibit energy back-transfer, thereby effectively confining triplet excitons on guest molecules.[22] Considering the triplet energy gaps of both **4a** and **5** (≈2.19 eV), the widely used host material 4,4′-*N*,*N*′-dicarbazolebiphenyl (CBP) was used,[23] which has a triplet energy gap of 2.56 eV and provides good exciton confinement on the present guest molecules. In addition, the photoluminescence of CBP overlaps well with both of the absorption spectra of our target phosphors, which facilitates the energy transfer from host to guest in the emitting layer. As a result, a series of devices were fabricated. The schematic structure of these devices and materials used are depicted in Figure 9, for which the indium tin oxide (ITO), α-naphthylphenylbiphenyl diamine (α-NPD), and Al were applied as the anode, the hole-transport layer (HTL), and the cathode, respectively. The architectures of the devices were ITO/α-NPD (40 nm)/CBP doped with 8 wt% of **4a** (series A) or **5** (series B) (30 nm)/BCP or TPBi or TAZ (40 nm)/LiF (0.5 nm)/Al (150 nm). Moreover, three electron-transport/hole-blocking materials commonly used in electrophosphorescence, namely 2,9-dimethyl-4,7-diphenyl-1,10-phenan-

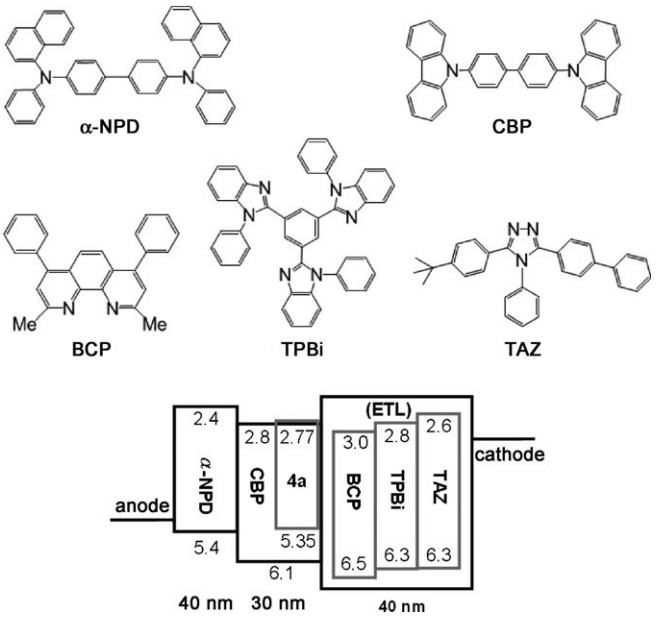

Figure 9. The chemical structures of materials and the energy-level diagram of the orange-emitting OLEDs.

throline (BCP, devices A1 and B1), 2,2′,2″-(1,3,5-benzenetriyl)-tris(1-phenyl-1-*H*-benzimidazole) (TPBi, devices A2 and B2) and 3-(4-biphenylyl)-4-phenyl-5-tert-butylphenyl-1,2,4-triazole (TAZ, devices A3 and B3),[24] were applied for examining the electron transport/hole blocking, charge/carrier balance and for optimizing the device performances. Finally, LiF was used as the electron-injection layer. The energy levels of different materials used in the devices (taken from references or those estimated from the cyclovoltammetry data of **4a** and **5**) are also marked in Figure 9 for reference.

The electroluminescence (EL) characteristics are summarized in Table 4, whereas the representative EL characteristics (EL spectra, current-voltage-brightness (*I-V-L*) and efficiencies) for devices A3 and B3 are depicted in Figure 10. As can be seen in Table 4, all devices A1–A3 showed the expected orange-red emission with $CIE_{x,y}$ of (0.55, 0.45; $CIE_{x,y}$ = the 1931 Commission Internationale de L'Eclairage (*x*,*y*) coordinates). This characteristic suggests that the emission is exclusively derived from phosphor **4a**, indicating efficient exothermic energy transfer from host to guest molecules and effective exciton confinement in the emitting layer. Note that the adoption of different electron-transporting materials has notable effects on the *I-V-L* characteristics. For example, higher current density and luminance were obtained in devices A1 (BCP) and A2 (TPBi), the results of which are perhaps associated with the higher electron mobilities of BCP and TPBi as well as the different capability in carrier injection.[25] On the other hand, a significantly higher peak external quantum efficiency of 14.6% photon/electron was obtained for the A3 device that employs the lower-mobility material, TAZ, for which the peak luminescence efficiency and the power efficiency went up to 34.8 cd A^{-1} and 26.1 Lm W^{-1}, respectively. At the practical brightness of

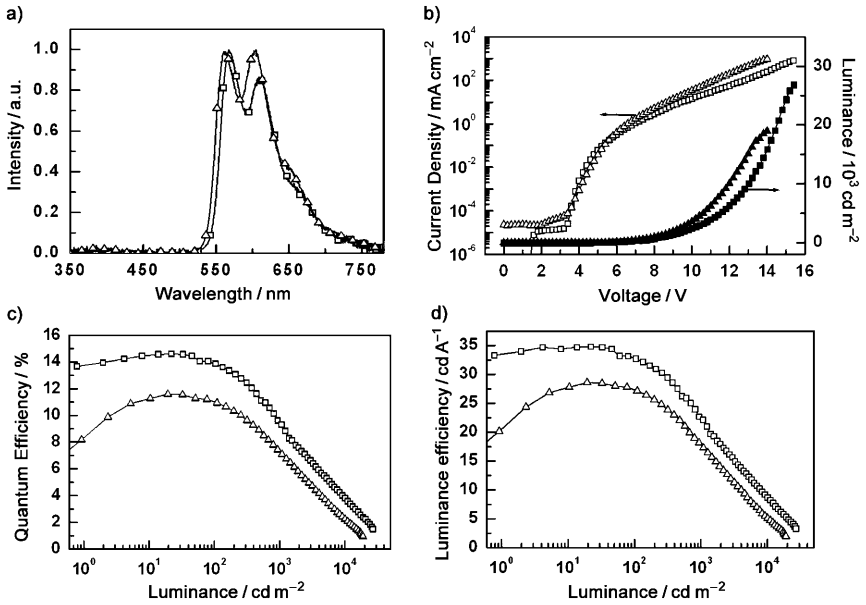

Figure 10. a) The EL spectra of devices A3 (□) and B3 (△) at 1000 cd/m^2; b) Current-voltage-luminance (*I-V-L*) characteristics of A3 (□, ■) and B3 (△, ▲); c) The external quantum efficiencies of devices A3 (□) and B3 (△); d) The luminance efficiencies of devices A3 (□) and B3 (△).

Table 4. EL characteristics of devices with different electron-transporting layers.

Device	EQE [%] [a]	EQE [%] [b]	LE [cd A^{-1}] [a]	LE [cd A^{-1}] [b]	PE [lm W^{-1}] [a]	PE [lm W^{-1}] [b]	Turn-on [V][c]	Max *L* [cd m^{-2}] ([V])	CIE[b]	CIE[d]
A1	10.6	10.4	26.0	25.2	16.8	12.8	4.0	41666 (13.4)	0.545, 0.452	0.545, 0.452
A2	10.4	10.3	25.2	24.9	19.3	12.6	3.8	40194 (13.4)	0.547, 0.450	0.547, 0.449
A3	14.6	13.9	34.8	32.7	26.1	17.1	4.0	26872 (15.4)	0.549, 0.449	0.549, 0.448
B1	7.5	7.4	18.8	18.6	10.6	9.4	4.4	25715 (12.8)	0.531, 0.459	0.529, 0.460
B2	7.5	7.4	18.3	18.2	10.0	9.9	4.4	26253 (12.8)	0.530, 0.458	0.528, 0.453
B3	11.6	10.9	28.6	27.1	17.6	14.2	4.4	18963 (14.0)	0.535, 0.460	0.533, 0.457

[a] Maximum efficiencies. [b] Measured at brightness of 100 cd m^{-2}. [c] Measured at brightness of 1 cd m^{-2}. [d] Measured at brightness of 1000 cd m^{-2}.

100 cd m^{-2}, the efficiencies of device A3 still remain about 13.9%, 32.7 cd A^{-1}, and 17.1 Lm W^{-1}, respectively. Such device results looked surprising at the first glance. Because the hole mobilities of α-NPD and CBP ($\geq 10^{-4}$ cm^2 V s)[26] are much higher than the electron mobility of TAZ ($\sim 10^{-6}$ cm^2 V s),[27] one would expect higher EL efficiencies from devices that use higher-electron-mobility BCP (A1) and TPBi (A2). A further examination of the energy levels of **4a** and CBP (Figure 9), however, reveals a large difference in ionization potentials between **4a** and CBP. Such a discrepancy in the energy-level alignment could result in hole trapping or hole-hopping transport on **4a** within the CBP layer, both of which would lower the hole-transport capability.[28] With such a scenario, in the current system, the low electron mobility of TAZ might alternatively provide a better condition for carrier balance in the emitting layer and thus for higher EL efficiencies. Of course, other subtle differences such as carrier injection from the electrode and into the emitting layer might also play a certain role in different device behaviors observed.

We also tested **5** as the emissive dopant (i.e., in the series B devices) for a fair comparison. These devices also exhibit emission predominantly from **5** (Figure 10). Again, device B3, which employed TAZ as the electron-transporting layer, gave the highest efficiencies among the devices that used the three different electron-transport materials (Figure 10, Table 4). The peak efficiencies for B3 are about 11.6%, 28.6 cd A^{-1} and 17.6 Lm W^{-1}, respectively. Although both **4a** and **5** are efficient emitters with similarly high PL quantum yields and similar emission color,[9] nevertheless in the present device structures, complex **5** exhibits significantly lower EL efficiencies. In Figure 10b, the lower voltage of the device B3 (vs. A3) at a same current or a same brightness can be noted, which indicates the differences in the carrier-transport properties of the **4a**- and **5**-doped CBP emitting layers. On the one hand, with only one pyrazolate chelate in **5**, the hole-trapping capability of the dopant might be reduced. More insightfully, on the other hand, we have made attempts to rationalize such a difference in transport properties by computing some parameters such as the ionization potentials (IP), electronic affinities (EA), and the reorganization energy (λ) to probe the intrinsic characters between complexes **4a** and **5**.[29] IP and EA are the parameters used to evaluate the tendency of injecting holes and electrons, respectively, the values of which are also directly related to the energy of HOMO and LUMO orbitals. On the other hand, λ could be used to assess the transport properties. As shown in Table 5, the IP for **4a**, which is defined by the energy difference between cation and neutral molecules (both with the optimized neutral geometry), is smaller than that for **5**, indicating that complex **4a** is more subject to hole injection from the hole-transport layer (HTL) and possesses better hole-trapping ability. Conversely, the higher EA for **4a** is better for accepting the electron injected from the electron-transport layer (ETL). These trends are also consistent with the order of the frontier orbital energy levels depicted in Figure 11.

Table 5. Calculated ionization potentials (IP), electron affinities (EA), and internal reorganization energy (λ) for complexes **4a** and **5**.

	IP [eV]	EA [eV]	λ_{hole} [eV]	λ_{elec} [eV]
4a	6.38	0.86	0.52	0.18
5	6.64	0.5	0.34	0.38

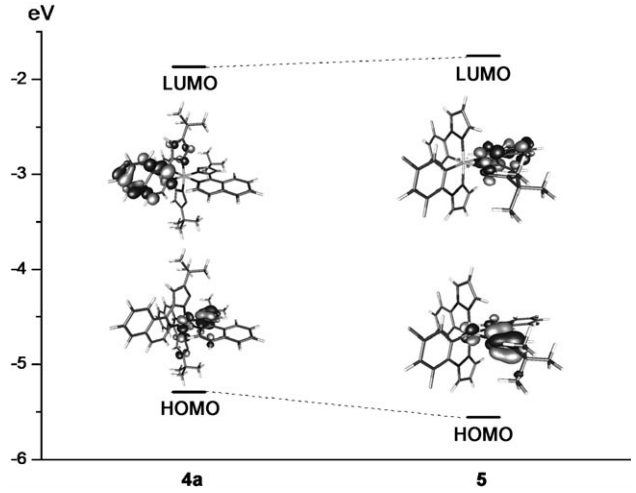

Figure 11. The frontier orbitals of complexes **4a** and **5**.

Both charge-transfer rate and balance have a significant influence on the EL efficiencies of the OLEDs device. Theoretically, these transport properties can be computed by using the simple Marcus/Hush model expressed as in [Eq. (1)], in which V denotes the coupling matrix element between the ions and molecules, and k_B stands for Boltzmann constant.[30]

$$k = (\frac{\pi}{\lambda k_B T})^{1/2} \frac{V^2}{\hbar} \exp(-\frac{\lambda}{4k_B T}) = A\exp(-\frac{\lambda}{4k_B T}) \quad (1)$$

The degree of charge transfer between molecules in the solid-state environment is rather weak and restricted, and can thus be ignored in this approach. Accordingly, the transport rate expressed in [Eq. (1)] solely depends on its internal reorganization energy without taking account of any other environmental relaxation and changes. As a result, the hole- and electron-transfer rate can be estimated by using [Eq. (2)] and [Eq. (3)], respectively.

$$\lambda_{hole} = \lambda^+ + \lambda^0 = [E^+(g^0) - E^+(g^+)] + [E^0(g^+) - E^0(g^0)] \quad (2)$$

$$\lambda_{elec} = \lambda^- + \lambda^0 = [E^-(g^0) - E^-(g^-)] + [E^0(g^-) - E^0(g^0)] \quad (3)$$

$E^+(g^0)$ and $E^+(g^+)$ represent the cation energy under optimized neutral and cation geometry, respectively, whereas $E^0(g^0)$ and $E^0(g^+)$ denote the neutral energy under optimized neutral and cation geometry, respectively. A similar definition applies for λ_{elec} except when using the minus su-

perscript. For a cation that is relevant to hole transport, Figure 12 qualitatively depicts the potential energy surface as a function of nuclear coordinate. The numerical data

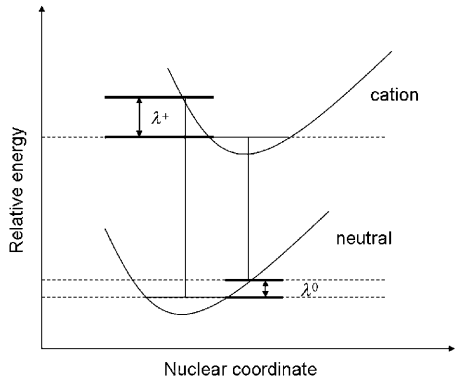

Figure 12. A qualitative depiction of the potential-energy surface for neutral and cationic species as a function of nuclear coordinate (see text for the definition of λ^+ and λ^0).

listed in Table 5 indicate that the larger λ_{hole} for **4a** reveals poor hole-transporting properties. Apparently, by using the relatively lower electron-mobility TAZ as the ETL can reduce the rate difference between holes and electrons, the result of which optimizes device performance effectively, giving better external quantum efficiency. As for complex **5**, the relatively low HOMO energy decreases its hole-trapping ability (smaller λ_{hole}), subtly altering the scenario of the carrier transport/balance and the exciton formation.

The above results reveal the interesting and subtle influences of ligating chromophores not only on the emission but also on the electrical characteristics of phosphors. Because both properties are critical in OLED devices, it in turn implies that in designing effective phosphors for PhOLEDs, not only the photophysical characteristics (colorant, quantum yields) but also their electrical behavior must be considered. Hence, these closely related designs provide a good example of how these may be fine-tuned through chelating architectures.

Conclusion

In summary, a rational design has been presented for a new series of homoleptic iridium(III) complexes, en route from the isolation of two intermediates **2a** and **b** and **3a** and **b** that both involve the coordination of two pyrazolate chelates as well as two terminal chlorides, to give the corresponding complexes with either a *cis*-Cl,Cl or a *trans*-Cl,Cl arrangement. Further conversion from these intermediates to the homoleptic, meridional **1a** and **1b** with tris(pyridyl pyrazolates) resulted in intermediates with similar structures being proposed en route to the formation of **4a** and **4b** with tris(isoquinolinyl pyrazolates). For complexes **1a** and **1b**, they demonstrate the unprecedented photophysical property of dual phosphorescence. The fast decay of the blue phosphorescence (P_1 band) at room temperature is attributed to the rapid conversion from T_{ILCT} to T_{LLCT} states followed by perhaps a $T_{LLCT} \rightarrow {}^3MC \rightarrow S_0$ deactivation process. The current result also agrees with previous reports for the related homoleptic Ir^{III} metal complexes such as *mer*- and *fac*-[Ir(dfppy)$_3$], ((dfppy)H = 4,6-difluorophenyl pyridine), in which the meridional isomer is always less emissive at room temperature compared with its facial counterpart under identical conditions.[31] We believe that a similar electron-transfer process is operative for *mer*-[Ir(dfppy)$_3$], which induces a rapid radiation-free deactivation pathway, giving poor emission at room temperature. We thus expect that the interplay between T_{ILCT} to T_{LLCT} may, in general, play a key role for spectroscopy and dynamics of the homoleptic-meridional types of transition-metal complexes.

As for the isoquinolinyl derivatives **4a** and **4b**, both showed bright-orange emission in the solid state, among which **4a** was selected as a prototype phosphor for the fabrication of phosphorescent OLEDs, showing the maximum external quantum efficiency as high as 14.6%. The respective performance data were superior to the OLEDs fabricated by using a related phosphor **5** with a single isoquinolinyl pyrazolate chromophore. These results also showed that not only the chromophoric ligand with the lowest energy gap, but also other ancillary ligands are important for controlling the efficiency and color of devices. The results would spark a broad spectrum of interest in the field of inorganic photochemistry and OLED research.

Experimental Section

General methods and materials: Mass spectra were obtained on a JEOL SX-102 A instrument operating in electron impact (EI) mode or fast atom bombardment (FAB) mode. ^{1}H and ^{13}C NMR spectra were recorded on Varian Mercury-400 or INOVA-500 instruments; chemical shifts are quoted with respect to the internal standard tetramethylsilane for ^{1}H and ^{13}C NMR data. Elemental analyses were carried out at the NSC Regional Instrumentation Center at National Chao Tung University, Hsinchu (Taiwan). The pyridyl pyrazole chelates, namely: 3-*tert*-butyl-5-(2-pyridyl) pyrazole (bppz)H, 3-trifluoromethyl-5-(2-pyridyl) pyrazole (fppz)H,[32] and their isoquinolyl derivatives, 3-*tert*-butyl-5-(1-isoquinolyl) pyrazole (bipz)H and 3-trifluoromethyl-5-(1-isoquinolyl) pyrazole (fipz)H[33] were prepared according to the literature procedures. All reactions were conducted under an N_2 atmosphere by using anhydrous solvents or solvents treated with an appropriate drying reagent.

Preparation of (1a): A suspension of sodium carbonate (372 mg, 1.85 mmol) was treated with (bppz)H (196 mg, 1.85 mmol) in diethylene glycol monoethyl ether (DGME, 25 mL). After stirring for 1 h, $IrCl_3 \cdot 3H_2O$ (185 mg, 0.53 mmol) was added and the solution was heated under reflux for 12 h. Excess water was added after cooling the solution to room temperature. The precipitate was filtered, purified by silica-gel column chromatography eluting with ethyl acetate, and crystallized from a mixture of CH_2Cl_2 and hexane at room temperature to render light-yellow *mer*-[Ir(bppz)$_3$] (**1a**, 222 mg, 0.28 mmol, yield = 53%). The derivative *mer*-[Ir(fppz)$_3$] (**1b**) was prepared by using a similar procedure (yield = 50%).

Spectral data of ***1a***: ^{1}H NMR (400 MHz, CD_2Cl_2, 294 K): δ = 7.73–7.63 (m, 5H; CH), 7.56 (d, J(H,H) = 7.6 Hz, 1H; CH), 7.43 (d, J(H,H) = 6.0 Hz, 1H; CH), 7.31 (d, J(H,H) = 6.0 Hz, 1H; CH), 6.94–6.90 (m, 3H;

CH), 6.85 (td, J(H,H) = 5.8, 2.0 Hz, 1H; CH), 6.59 (s, 1H; CH), 6.55 (s, 1H; CH), 6.50 (s, 1H; CH), 1.34 (s, 9H; CH_3), 1.29 (s, 9H; CH_3), 1.24 ppm (s, 9H; CH_3); MS (FAB, ^{193}Ir): m/z: 793 $[M]^+$, 593 $[M-\text{bppz}]^+$; elemental analysis calcd (%) for $C_{36}H_{42}IrN_9$: N 15.90, C 54.53, H 5.34; found: N 16.02, C 54.82, H 5.01.

Spectral data of ***1b***: ^{1}H NMR (500 MHz, [D$_6$]acetone, 294 K): δ = 8.22 (td, J(H,H) = 6.0, 0.8 Hz, 1H; CH), 8.14–7.97 (m, 5H; CH), 7.74 (td, J(H,H) = 6.0, 0.8 Hz, 1H; CH), 7.48 (td, J(H,H) = 6.0, 0.8 Hz, 1H; CH), 7.42 (ddd, J(H,H) = 7.4, 5.0, 1.2 Hz, 1H; CH), 7.34 (m, 1H; CH), 7.31 (s, 1H; CH), 7.28 (ddd, J(H,H) = 7.4, 5.0, 2.0 Hz, 1H; CH), 7.25(s, 1H; CH), 7.20 (ddd, J(H,H) = 7.4, 5.0, 1.2 Hz, 1H; CH), 7.13 ppm (s, 1H; CH); ^{19}F NMR (470 MHz, [D$_6$]acetone): δ = −59.80 (s, 3F; CF_3), −60.00 (s, 3F; CF_3), −60.05 (s, 3F; CF_3); MS (FAB, ^{193}Ir): m/z: 830 $[M]^+$, 618 $[M-\text{fppz}]^+$; elemental analysis calcd (%) for $C_{27}H_{15}F_9IrN_9$: N 15.21, C 39.13, H 1.82; found: N 15.42, C 40.02, H 2.01.

***cis*-[Ir(bppz)$_2$Cl$_2$]H (2a) and *trans*-[Ir(bppz)$_2$Cl$_2$]H (3a)**: A 50 mL reaction flask was charged with (bppz)H (483 mg, 2.40 mmol), $IrCl_3$ (390 mg, 1.1 mmol), and 2-methoxyethanol (20 mL), and the resulting mixture was heated under reflux for 12 h. After cooling to RT and removal of the solvent, the residue was separated by silica-gel column chromatography eluting with ethyl acetate, and crystallized from methanol to afford two light-yellow components corresponding to *cis*-[Ir(bppz)$_2$Cl$_2$]H (**2a**, 408 mg, 0.61 mmol, yield = 55%) and *trans*-[Ir(bppz)$_2$Cl$_2$]H (**3a**, 36 mg, 0.056 mmol, yield = 5%).

Spectral data of ***2a***: ^{1}H NMR (400 MHz, $CDCl_3$, 294 K): δ = 9.58 (d, J(H,H) = 6.0 Hz, 1H; CH), 7.78 (t, J(H,H) = 7.4 Hz, 1H; CH), 7.73 (d, J(H,H) = 8.0 Hz, 1H; CH), 7.67–7.62 (m, 2H; CH), 7.39 (d, J(H,H) = 6.0 Hz, 1H; CH), 7.22 (t, J(H,H) = 6.0 Hz, 1H; CH), 6.98 (td, J(H,H) = 7.2, 1.2 Hz, 1H; CH), 6.69 (s, 1H; CH), 6.35 (s, 1H; CH), 1.51 (s, 9H; CH_3), 1.12 ppm (s, 9H; CH_3); MS (FAB, ^{193}Ir): m/z: 666 $[M]^+$; elemental analysis calcd (%) for $C_{24}H_{29}IrCl_2N_6$: N 12.64, C 43.37, H 4.40; found: N 12.51, C 43.62, H 4.92.

Selected crystal data of ***2a***: $C_{24}H_{29}Cl_2IrN_6{\cdot}H_2O$; M_r = 682.64; monoclinic; space group = Cc; a = 11.6739(11), b = 39.942(4), c = 12.2437(12) Å; β = 114.772(2)°; V = 5183.7(9) Å^3; Z = 8; ρ_{calcd} = 1.747 mg m^{-3}; $F(000)$ = 2680; crystal size = 0.14 × 0.05 × 0.05 mm^3; $\lambda(Mo_{K\alpha})$ = 0.7107 Å; T = 150(2) K; μ = 5.386 mm^{-1}; 24017 reflections collected; 11363 independent reflections (R_{int} = 0.0600); GOF = 0.994; final $R_1[I>2\sigma(I)]$ = 0.0475; wR_2(all data) = 0.0930.

Spectral data of ***3a***: ^{1}H NMR (500 Hz, $CDCl_3$, 298 K): δ = 9.07 (d, J(H,H) = 5.6 Hz, 2H; CH), 7.86–7.81 (m, 4H; CH), 7.39 (t, J(H,H) = 5.6 Hz, 2H; CH), 6.58 (s, 2H; CH), 1.51 ppm (s, 18H; CH_3); MS (FAB, ^{193}Ir): m/z: 665 $[M]^+$, 630 $[M-\text{Cl}]^+$; elemental analysis calcd (%) for $C_{24}H_{29}Cl_2IrN_6$: N 12.64, C 43.37 H 4.40; found: N 12.24, C 43.15, H 4.78.

***cis*-[Ir(fppz)$_2$Cl$_2$]H (2b) and *trans*-[Ir(fppz)$_2$Cl$_2$]H (3b)**: The products *cis*-[Ir(fppz)$_2$Cl$_2$]H (**2b**, yield = 31%) and *trans*-[Ir(fppz)$_2$Cl$_2$]H (**3b**, yield = 19%) were prepared by using a procedure similar to that reported for *tert*-butyl derivatives **2a** and **3a**. Single crystals of *cis*-[Ir(fppz)$_2$Cl$_2$]H and *trans*-[Ir(fppz)$_2$Cl$_2$]H were obtained after repeated recrystallization from acetone at room temperature.

Spectral data of ***2b***: ^{1}H NMR (500 MHz, [D$_6$]acetone, 294 K): δ = 9.67 (d, J(H,H) = 5.5 Hz, 1H; CH), 8.13–8.07 (m, 2H; CH), 7.94 (d, J(H,H) = 7.0 Hz, 1H; CH), 7.78 (td, J(H,H) = 7.0, 1.0 Hz, 1H; CH), 7.57 (td, J(H,H) = 6.0, 2.0 Hz, 1H; CH), 7.52 (d, J(H,H) = 5.5 Hz, 1H; CH), 7.20 (s, 1H; CH), 7.05–7.02 ppm (m, 2H; CH); ^{19}F NMR (470 MHz, [D$_6$]acetone, 294 K): δ = −60.5 (s, 3F; CF_3), −60.3 (s, 3F; CF_3); MS (FAB, ^{193}Ir): m/z: 733 $[M]^+$; elemental analysis calcd (%) for $C_{18}H_{11}Cl_2IrF_6N_6$: N 12.21, C 31.40, H 1.61; found: N 12.04, C 31.55, H 2.09.

Spectral data of ***3b***: ^{1}H NMR (500 Hz, [D$_6$]acetone, 298 K): δ = 9.51 (d, J(H,H) = 6.0 Hz, 2H; CH), 8.38 (d, J(H,H) = 8.0 Hz, 2H; CH), 8.26 (td, J(H,H) = 8.5, 1.0 Hz, 2H; CH), 7.78 (td, J(H,H) = 6.5, 1.5 Hz, 2H; CH), 7.66 ppm (s, 2H; CH); ^{19}F NMR (470 MHz, [D$_6$]acetone, 294 K): δ = −61.5 ppm (s, 6F; CF_3); MS (FAB, ^{193}Ir): m/z: 688 $[M]^+$, 653 $[M-\text{Cl}]^+$, 617 $[M-2\text{Cl}]^+$; elemental analysis calcd (%) for $C_{18}H_{11}Cl_2IrF_6N_6$: N 12.21, C 31.40, H 1.61; found: N 12.10, C 31.50, H 2.04.

Selected crystal data of ***3b***: $C_{18}H_{11}Cl_2F_6IrN_6{\cdot}C_3H_6O$; M_r = 746.50; orthorhombic; space group = $P2_12_12_1$; a = 11.9562(9), b = 14.0045(10), c = 14.4648(11); V = 2422.0(3) Å^3; Z = 4; ρ_{calcd} = 2.044 mg m^{-3}; $F(000)$ = 1428; crystal size = 0.20 × 0.15 × 0.15 mm^3; $\lambda(Mo_{K\alpha})$ = 0.7107 Å; T = 150(2) K; μ = 5.808 mm^{-1}; 15783 reflections collected; 5545 independent reflections (R_{int} = 0.0428); GOF = 1.033; final $R_1[I>2\sigma(I)]$ = 0.0339; wR_2(all data) = 0.0760.

Alternative synthesis of *mer*-[Ir(bppz)$_3$] (1a): A mixture of *cis*-[Ir(bppz)$_2$Cl$_2$]H (100 mg, 0.15 mmol), (bppz)H (45 mg, 0.22 mmol), and Na_2CO_3 (47 mg, 0.44 mmol) in 2-methoxyethanol (15 mL) was heated under reflux for 12 h. Excess water was added after cooling the solution to room temperature. The precipitate was filtered, purified by using silica-gel column chromatography eluting with ethyl acetate, and crystallized from a mixed solvent of CH_2Cl_2 and hexane at room temperature to render light-yellow crystals (66 mg, 0.08 mmol, yield = 56%).

Preparation of *mer*-[Ir(bipz)$_3$] (4a): A suspension of sodium carbonate (982 mg, 9.27 mmol) was treated with (bipz)H (1.17 g, 4.69 mmol) in DGME (20 mL). After stirring for 1 h, $IrCl_3{\cdot}3H_2O$ (412 mg, 1.17 mmol) was added and the resulting mixture was heated under reflux for 12 h. Then excess water was added to precipitate an orange powder. This precipitate was further purified by silica-gel column chromatography eluting with ethyl ether, and was crystallized from a mixture of CH_2Cl_2 and methanol at room temperature (**4a**, 769 mg, 0.81 mmol, yield = 68.6%).

Spectral data of ***4a***: ^{1}H NMR (500 MHz, [D$_6$]acetone, 294 K): δ = 8.98 (t, J_{HH} = 5.0 Hz, 1H; CH), 8.94 (t, J(H,H) = 5.0 Hz, 1H; CH), 8.90 (d, J(H,H) = 8.5 Hz, 1H; CH), 7.93–7.87 (m, 2H; CH), 7.81–7.78 (m, 3H; CH), 7.75–7.69 (m, 4H; CH), 7.59 (d, J(H,H) = 6.5 Hz, 1H; CH), 7.48 (d, J(H,H) = 6.5 Hz, 1H; CH), 7.35 (d, J(H,H) = 6.5 Hz, 1H; CH), 7.25–7.30 (m, 2H; CH), 7.22 (s, 1H; CH), 7.20 (s, 1H; CH), 7.06 (s, 1H; CH), 6.93 (d, J(H,H) = 6.0 Hz, 1H; CH), 1.29 (s, 9H; CH_3), 1.27 (s, 9H; CH_3), 1.22 ppm (s, 9H; CH_3); MS (FAB, ^{193}Ir): m/z: 945 $[M]^+$, 694 $[M-\text{bipz}]^+$; elemental analysis calcd (%) for $C_{48}H_{48}IrN_9$: N 13.37, C 61.12, H 5.13; found: N 13.43, C 60.71, H 5.27.

Selected crystal data of ***4a***: $C_{49}H_{52}Cl_2N_9OIr$; M_r = 1046.10; monoclinic; space group = Cc; a = 22.8643(6), b = 11.1614(3), c = 19.5508(5) Å; β = 109.2683(16)°; V = 4709.8(2) Å^3; Z = 4; ρ_{calcd} = 1.475 mg m^{-3}; $F(000)$ = 2112; crystal size = 0.35 × 0.05 × 0.04 mm^3; $\lambda(Mo_{K\alpha})$ = 0.7107 Å; T = 295(1) K; μ = 2.995 mm^{-1}; 24682 reflections collected; 8496 independent reflections (R_{int} = 0.0618); GOF = 1.006; final R_1 $[I>2\sigma(I)]$ = 0.0418; wR_2 (all data) = 0.0906.

Preparation of *mer*-[Ir(fipz)$_3$] (4b): The derivative **4b** was prepared in 62% yield by using procedures reported for the *tert*-butyl analogue **4a**.

Spectral data of ***4b***: ^{1}H NMR (500 MHz, $CDCl_3$, 294 K): δ = 8.77 (t, J(H,H) = 3.0 Hz, 1H; CH), 8.66 (d, J(H,H) = 7.5 Hz, 2H; CH), 7.85–7.83 (m, 1H; CH), 7.80–7.78 (m, 2H; CH), 7.69–7.62 (m, 5H; CH), 7.46–7.44 (m, 3H; CH), 7.37 (s, 1H; CH), 7.31 (d, J(H,H) = 3.0 Hz, 2H; CH), 7.24 (t, J(H,H) = 2.5 Hz, 2H; CH), 7.16 (d, J(H,H) = 6.5 Hz, 1H; CH), 7.11 ppm (d, J(H,H) = 6.0 Hz, 1H; CH); ^{19}F NMR (470 MHz, $CDCl_3$): δ = −60.23 (s, 3F; CF_3), −60.26(s, 3F; CF_3), −60.42 ppm (s, 3F; CF_3); MS (FAB, ^{193}Ir): m/z: 978 $[M]^+$; elemental analysis calcd (%) for $C_{39}H_{21}IrF_9N_9$: N 12.88, C 47.85, H 2.16; found: N 12.92, C 48.01, H 2.23.

X-ray diffraction studies: Single-crystal X-ray diffraction data were measured on a Bruker SMART Apex CCD diffractometer using ($Mo_{K\alpha}$) radiation (λ = 0.71073 Å). The data collection was executed by using the SMART program. Cell refinement and data reduction were performed with the SAINT program. The structure was determined by using the SHELXTL/PC program and was refined by using full-matrix least squares analysis. CCDC-753561 (**2a**), 753560 (**3b**), and 753559 (**4a**) contain the supplementary crystallographic data for this paper. These data can be obtained free of charge from The Cambridge Crystallographic Data Centre via www.ccdc.cam.ac.uk/data_request/cif.

Photophysical data measurement and OLED fabrication: Steady-state absorption, emission, and phosphorescence lifetime measurements both in solution and in the solid state have been described in our previous reports.[34] For measuring quantum yields in the solid state, an integrating sphere (Labsphere) was used. The solid film was prepared by using a vapor-deposition method and was excited by a 514 nm Ar^+ laser line. The emission was then acquired by an intensified charge-coupled detector for subsequent analyses.[35] The fabrication procedures for the OLED

devices including those for patterning and cleaning of ITO substrates followed those described in the literature.[36]

Computational methodology: Calculations on electronic singlet and triplet states of complexes **1a**, **1b** and **4a**, **4b** were carried out by using a hybrid Hartree–Fock/density functional model (PBE1PBE) based on the Perdew-Burke-Erzenrhof (PBE) functional.[37] Restricted and unrestricted formalisms were adopted in the singlet and triplet geometry optimization, respectively. A "double-ζ" quality basis set consisting of Hay and Wadt's effective core potentials (LANL2DZ)[38] was employed for the Ir atom, and a 6-31G* basis set[39] was employed for H, C, N, and F atoms. The relativistic effective core potential (ECP) replaced the inner core electrons of Ir^{III} metal atom, leaving the outer core ($5s^25p^6$) electrons and the $5d^6$ valence electrons to be concerned. TDDFT calculations by using the PBE0 functional were then performed[40] based on the optimized structures at ground states in combination with an integral equation formalism-polarizable continuum model in dichloromethane (IEF-PCM), implemented in Gaussian 03.[41] Typically, the lowest triplet and singlet roots of the nonhermitian eigenvalue equations were obtained to determine the vertical excitation energies. Oscillator strengths were deduced from the dipole transition matrix elements (for singlet states only). All calculations were carried out by using Gaussian 03.[42]

The electronic configurations of ^{3}MC dd states were calculated following the literature methodology.[20] The ^{3}MLCT state geometry was obtained by performing geometry optimization along the triplet state potential-energy surface (PES) by using the X-ray structural data as the initial geometry. As for the ^{3}MC state, because the electron densities are mainly distributed on the central metal atom, the chelating interaction between metal and ligands must be rather weak. We thus performed geometry optimization of the ^{3}MC state following the methodology illustrated in the work of Persson et al.[20] The method starting with a distorted geometry, for which the metal–ligand bonds are largely elongated, such that its associated energy is expected to be far away from the global minimum along the PES. Based on this methodology, the optimization is then able to fall into the presumably shallow local minimum associated with the ^{3}MC dd excited state. The resulting ^{3}MC dd excited state structure was then confirmed by the net spin values located on the transition metal from the Mulliken population analysis. The frontier orbitals and net spin values of the ^{3}MC dd state for complexes **1b** and **4b** are depicted in the Supporting Information for reference (Figures S3 and S4).

Compositions of molecular orbitals in terms of the constituent chemical fragments were calculated by using the AOMix program.[43] For the characterization of the HOMO$-x$→LUMO$+y$ transitions as partial charge-transfer (CT) transitions, the definition of the CT character in [Eq. (4)] has been used in which %(M)HOMO$-x$ and %(M)LUMO$+y$ are electronic densities on the metal in HOMO$-x$ and LUMO$+y$, respectively.

$$\mathrm{CT(M)} = \%\mathrm{(M)HOMO}-x-\%\mathrm{(M)LUMO}-y \quad (4)$$

If the excited state (e.g., S_1 or T_1) is formed by more than one one-electron excitation, then the metal CT character of this excited state is expressed as a sum of CT characters of each participating excitation, $i \rightarrow j$, as shown in [Eq. (5)] in which C_I ($i \rightarrow j$) are the appropriate coefficients of the **I**th eigenvector of the CI matrix.

$$\mathrm{CT_I(M)} = \sum_{i,\mathrm{a}} [C_I(i \rightarrow j)]^2 (\%(\mathrm{M})_i - \%(\mathrm{M})_j) \quad (5)$$

Accordingly, one can very effectively use the MO compositions in terms of fragment orbital contributions to probe the nature of the electronic transitions.

Acknowledgements

This work was supported by the National Science Council and Ministry of Economic Affairs of Taiwan.

[1] a) H. Yersin, *Top. Curr. Chem.* **2004**, *241*, 1–26; b) S.-W. Lai, C.-M. Che, *Top. Curr. Chem.* **2004**, *241*, 27–63; c) R. C. Evans, P. Douglas, C. J. Winscom, *Coord. Chem. Rev.* **2006**, *250*, 2093–2126; d) M. K. Nazeeruddin, M. Gratzel, *Struct. Bonding (Berlin)* **2007**, *123*, 113–175; e) P.-T. Chou, Y. Chi, *Chem. Eur. J.* **2007**, *13*, 380–395; f) P.-T. Chou, Y. Chi, *Eur. J. Inorg. Chem.* **2006**, 3319–3332; g) Y. You, S. Y. Park, *Dalton Trans.* **2009**, 1267–1282; h) W.-Y. Wong, C.-L. Ho, *J. Mater. Chem.* **2009**, *19*, 4457–4482.

[2] a) A. B. Tamayo, S. Garon, T. Sajoto, P. I. Djurovich, I. M. Tsyba, R. Bau, M. E. Thompson, *Inorg. Chem.* **2005**, *44*, 8723–8732; b) F.-M. Hwang, H.-Y. Chen, P.-S. Chen, C.-S. Liu, Y. Chi, C.-F. Shu, F.-I. Wu, P.-T. Chou, S.-M. Peng, G.-H. Lee, *Inorg. Chem.* **2005**, *44*, 1344–1353; c) T. Matsushita, T. Asada, S. Koseki, *J. Phys. Chem. C* **2007**, *111*, 6897–6903; d) G. Zhou, C.-L. Ho, W.-Y. Wong, Q. Wang, D. Ma, L. Wang, Z. Lin, T. B. Marder, A. Beeby, *Adv. Funct. Mater.* **2008**, *18*, 499–511.

[3] a) I. M. Dixon, J.-P. Collin, J.-P. Sauvage, L. Flamigni, S. Encinas, F. Barigelletti, *Chem. Soc. Rev.* **2000**, *29*, 385; b) K. Dedeian, J. Shi, N. Shepherd, E. Forsythe, D. C. Morton, *Inorg. Chem.* **2005**, *44*, 4445–4447; c) Y. Chi, P.-T. Chou, *Chem. Soc. Rev.* **2010**, *39*, 638–655.

[4] a) S. Lamansky, P. Djurovich, D. Murphy, F. Abdel-Razzaq, H.-E. Lee, C. Adachi, P. E. Burrows, S. R. Forrest, M. E. Thompson, *J. Am. Chem. Soc.* **2001**, *123*, 4304–4312; b) S. Lamansky, P. Djurovich, D. Murphy, F. Abdel-Razzaq, R. Kwong, I. Tsyba, M. Bortz, B. Mui, R. Bau, M. E. Thompson, *Inorg. Chem.* **2001**, *40*, 1704–1711.

[5] a) M. K. DeArmond, J. E. Hillis, *J. Chem. Phys.* **1968**, *49*, 466–467; b) G. A. Crosby, R. J. Watts, S. J. Westlake, *J. Chem. Phys.* **1971**, *55*, 4663–4664.

[6] a) R. Ballardini, G. Varani, M. T. Indelli, F. Scandola, *Inorg. Chem.* **1986**, *25*, 3858–3865; b) W. Cheng, *J. Coord. Chem.* **1983**, *13*, 57–62.

[7] S. Basu, S.-M. Peng, G.-H. Lee, S. Bhattacharya, *Polyhedron* **2005**, *24*, 157–163.

[8] Y.-S. Yeh, Y.-M. Cheng, P.-T. Chou, G.-H. Lee, C.-H. Yang, Y. Chi, C.-F. Shu, C.-H. Wang, *ChemPhysChem* **2006**, *7*, 2294–2297.

[9] C.-J. Chang, C.-H. Yang, K. Chen, Y. Chi, C.-F. Shu, M.-L. Ho, Y.-S. Yeh, P.-T. Chou, *Dalton Trans.* **2007**, 1881–1990.

[10] a) S. Bettington, A. L. Thompson, A. Beeby, A. E. Goeta, *Acta Crystallogr. Sect. E* **2004**, *60*, m827–m829; b) L.-Q. Chen, C.-L. Yang, J.-G. Qin, *Acta Crystallogr. Sect. C* **2005**, *61*, m513–m515.

[11] B. Liang, C. Jiang, Z. Chen, X. Zhang, H. Shi, Y. Cao, *J. Mater. Chem.* **2006**, *16*, 1281–1286.

[12] K. Dedeian, P. I. Djurovich, F. O. Garces, G. Carlson, R. J. Watts, *Inorg. Chem.* **1991**, *30*, 1685–1687.

[13] K.-C. Hwang, J.-L. Chen, Y. Chi, C.-W. Lin, Y.-M. Cheng, G.-H. Lee, P.-T. Chou, S.-Y. Lin, C.-F. Shu, *Inorg. Chem.* **2008**, *47*, 3307–3317.

[14] a) F.-C. Hsu, Y.-L. Tung, Y. Chi, C.-C. Hsu, Y.-M. Cheng, M.-L. Ho, P.-T. Chou, S.-M. Peng, A. J. Carty, *Inorg. Chem.* **2006**, *45*, 10188–10196; b) J.-K. Yu, Y.-H. Hu, Y.-M. Cheng, P.-T. Chou, S.-M. Peng, G.-H. Lee, A. J. Carty, Y.-L. Tung, S.-W. Lee, Y. Chi, C.-S. Liu, *Chem. Eur. J.* **2004**, *10*, 6255–6264; c) P.-C. Wu, J.-K. Yu, Y.-H. Song, Y. Chi, P.-T. Chou, S.-M. Peng, G.-H. Lee, *Organometallics* **2003**, *22*, 4938–4946.

[15] a) S.-Y. Chang, J. Kavitha, J.-Y. Hung, Y. Chi, Y.-M. Cheng, E. Y. Li, P.-T. Chou, G.-H. Lee, A. J. Carty, *Inorg. Chem.* **2007**, *46*, 7064–7074; b) S.-Y. Chang, J.-L. Chen, Y. Chi, Y.-M. Cheng, G.-H. Lee, C.-M. Jiang, P.-T. Chou, *Inorg. Chem.* **2007**, *46*, 11202–11212.

[16] Y.-H. Song, S.-J. Yeh, C.-T. Chen, Y. Chi, C.-S. Liu, J.-K. Yu, Y.-H. Hu, P.-T. Chou, S.-M. Peng, G.-H. Lee, *Adv. Funct. Mater.* **2004**, *14*, 1221–1226.

[17] a) Y.-L. Tung, P.-C. Wu, C.-S. Liu, Y. Chi, J.-K. Yu, Y.-H. Hu, P.-T. Chou, S.-M. Peng, G.-H. Lee, Y. Tao, A. J. Carty, C.-F. Shu, F.-I. Wu, *Organometallics* **2004**, *23*, 3745–3748; b) Y.-M. Cheng, G.-H. Lee, P.-T. Chou, L.-S. Chen, Y. Chi, C.-H. Yang, Y.-H. Song, S.-Y. Chang, P.-I. Shih, C.-F. Shu, *Adv. Funct. Mater.* **2008**, *18*, 183–194.

[18] a) Y.-H. Song, S.-J. Yeh, C.-T. Chen, Y. Chi, C.-S. Liu, J.-K. Yu, Y.-H. Hu, P.-T. Chou, S.-M. Peng, G.-H. Lee, *Adv. Funct. Mater.* **2004**, *14*, 1221–1226; b) C. S. K. Mak, A. Hayer, S. I. Pascu, S. E. Watkins,

A. B. Holmes, A. Koehler, R. H. Friend, *Chem. Commun.* **2005**, 4708–4710.

[19] a) L. Hammarström, F. Barigelletti, L. Flamigni, M. T. Indelli, N. Armaroli, G. Calogero, M. Guardigli, A. Sour, J. P. Collin, J. P. Sauvage, *J. Phys. Chem. A* **1997**, *101*, 9061–9069; b) M. I. J. Polson, F. Loiseau, S. Campagna, G. S. Hanan, *Chem. Commun.* **2006**, 1301–1303; c) M. I. J. Polson, E. A. Medlycott, G. S. Hanan, L. Mikelsons, N. L. Taylor, M. Watanabe, Y. Tanaka, F. Loiseau, R. Passalacqua, S. Campagna, *Chem. Eur. J.* **2004**, *10*, 3640–3648; d) Y.-Q. Fang, N. J. Taylor, G. S. Hanan, F. Loiseau, R. Passalacqua, S. Campagna, H. Nierengarten, A. Van Dorsselaer, *J. Am. Chem. Soc.* **2002**, *124*, 7912–7913; e) S. Encinas, L. Flamigni, F. Barigelletti, E. C. Constable, C. E. Housecroft, E. R. Schofield, E. Figgemeier, D. Fenske, M. Neuburger, J. G. Vos, M. Zehnder, *Chem. Eur. J.* **2002**, *8*, 137–150; f) P. Ceroni, A. Credi, V. Balzani, S. Campagna, G. S. Hanan, C. R. Arana, J. M. Lehn, *Eur. J. Inorg. Chem.* **1999**, 1409–1414; g) M. Hissler, A. El-ghayoury, A. Harriman, R. Ziessel, *Angew. Chem.* **1998**, *110*, 1804–1807; *Angew. Chem. Int. Ed.* **1998**, *37*, 1717–1720.

[20] a) T. Bark, R. P. Thummel, *Inorg. Chem.* **2005**, *44*, 8733–8739; b) M. Abrahamsson, M. J. Lundqvist, H. Wolpher, O. Johansson, L. Eriksson, J. Bergquist, T. Rasmussen, H.-C. Becker, L. Hammarström, P.-O. Norrby, B. Åkermark, P. Persson, *Inorg. Chem.* **2008**, *47*, 3540–3548.

[21] Y.-L. Tung, L.-S. Chen, Y. Chi, P.-T. Chou, Y.-M. Cheng, E. Y. Li, G.-H. Lee, C.-F. Shu, F.-I. Wu, A. J. Carty, *Adv. Funct. Mater.* **2006**, *16*, 1615–1626.

[22] R. J. Holmes, S. R. Forrest, Y.-J. Tung, R. C. Kwong, J. J. Brown, S. Garon, M. E. Thompson, *Appl. Phys. Lett.* **2003**, *82*, 2422–2424.

[23] a) M. A. Baldo, S. Lamansky, P. E. Burrows, M. E. Thompson, S. R. Forrest, *Appl. Phys. Lett.* **1999**, *75*, 4–6; b) C. Adachi, R. Kwong, S. R. Forrest, *Org. Electron.* **2001**, *2*, 37–43; c) C. Adachi, M. A. Baldo, S. R. Forrest, S. Lamansky. M. E. Thompson, R. C. Kwong, *Appl. Phys. Lett.* **2001**, *78*, 1622–1624.

[24] a) V. I. Adamovich, S. R. Cordero, P. I. Djurovich, A. Tamayo, M. E. Thompson, B. W. D′Andrade, S. R. Forrest, *Org. Electron.* **2003**, *4*, 77–87; b) C.-C. Wu, Y.-T. Lin, K.-T. Wong, R.-T. Chen, Y.-Y. Chien, *Adv. Mater.* **2004**, *16*, 61–65; c) M.-H. Tsai, H.-W. Lin, H.-C. Su, T.-H. Ke, C.-C. Wu, F.-C. Fang, Y.-L. Liao, K.-T. Wong, C.-I Wu, *Adv. Mater.* **2006**, *18*, 1216–1220.

[25] a) W.-Y. Hung, T.-H. Ke, Y.-T. Lin, C.-C. Wu, T.-H. Hung, T.-C. Chao, K.-T. Wong, C.-I. Wu, *Appl. Phys. Lett.* **2006**, *88*, 0641021–0641023; b) T. Yasuda, Y. Yamaguchi, D.-C. Zou, T. Tsutsui, *Jpn. J. Appl. Phys. Part 1* **2002**, *41*, 5626–5629.

[26] a) N. Matsusue, Y. Suzuki, H. Naito, *Jpn. J. Appl. Phys.* **2005**, *44*, 3691–3694; b) S. C. Tse, K. C. Kwok, S. K. So, *Appl. Phys. Lett.* **2006**, *89*, 2621021–2621023.

[27] The electron mobility of TAZ was measured by the time-of-flight (TOF) transient photocurrent technique with the device: glass/Ag (30 nm)/TAZ ($\approx$2 μm)/Al (150 nm). Pulsed illumination (third harmonic of Nd:YAG laser, 355 nm, 10 ns) through the semitransparent electrode (Ag) induces generation of a thin sheet of excess carriers. Depending on the polarity of the applied bias (V), photogenerated carriers (or electrons) are swept across the sample with thickness D, the time required for sweeping across the sample with thickness D is t_T and the carrier mobility is thus given by $\mu = D^2/(Vt_T)$.

[28] a) H. Aziz, Z. D. Popovic, *Appl. Phys. Lett.* **2002**, *80*, 2180; b) N. von Malm, J. Steiger, R. Schmechel, H. von Seggern, *J. Appl. Phys.* **2001**, *89*, 5559–5563; c) Y. Kim, E. Oh, H. Lim, C.-S. Ha, *Appl. Phys. Lett.* **2006**, *88*, 0435041–1435043; d) V. V. Jarikov, *Appl. Phys. Lett.* **2008**, *92*, 244103.

[29] a) X.-N. Li, Z.-J. Wu, Z.-J. Si, H.-J. Zhang, L. Zhou, X.-J. Liu, *Inorg. Chem.* **2009**, *48*, 7740–7749; b) H. Gao, C. Qin, H. Zhang, S. Wu, Z.-M. Su, Y. Wang, *J. Phys. Chem. A* **2008**, *112*, 9097–9103.

[30] a) N. S. Hush, *J. Chem. Phys.* **1958**, *28*, 962–972; b) R. A. Marcus, *Rev. Mod. Phys.* **1993**, *65*, 599; c) R. A. Marcus, *J. Chem. Phys.* **1956**, *24*, 966–979.

[31] a) A. B. Tamayo, B. D. Alleyne, P. I. Djurovich, S. Lamansky, I. Tsyba, N. N. Ho, R. Bau, M. E. Thompson, *J. Am. Chem. Soc.* **2003**, *125*, 7377–7387; b) T. Karatsu, T. Nakamura, S. Yagai, A. Kitamura, K. Yamaguchi, Y. Matsushima, T. Iwata, Y. Hori, T. Hagiwara, *Chem. Lett.* **2003**, *32*, 886–887.

[32] C.-C. Cheng, W.-S. Yu, P.-T. Chou, S.-M. Peng, G.-H. Lee, P.-C. Wu, Y.-H. Song, Y. Chi, *Chem. Commun.* **2003**, 2628–2629.

[33] Y. L. Tung, S. W. Lee, Y. Chi, L. S. Chen, C. F. Shu, F. I. Wu, A. J. Carty, P. T. Chou, S. M. Peng, G. H. Lee, *Adv. Mater.* **2005**, *17*, 1059–1064.

[34] P. T. Chou, W. S. Yu, Y. M. Cheng, S. C. Pu, Y. C. Yu, Y. C. Lin, C. H. Huang, C. T. Chen, *J. Phys. Chem. A* **2004**, *108*, 6487–6498.

[35] J. C. de Mello, H. F. Wittmann, R. H. Friend, *Adv. Mater.* **1997**, *9*, 230–232.

[36] M.-H. Tsai, Y.-H. Hong, C.-H. Chang, H.-C. Su, C.-C. Wu, A. Matoliukstyte, J. Simokaitiene, S. Grigalevicius, J. V. Grazulevicius, C.-P. Hsu, *Adv. Mater.* **2007**, *19*, 862–866.

[37] a) J. P. Perdew, K. Burke, M. Ernzerhof, *Phys. Rev. Lett.* **1996**, *77*, 3865–3868; b) J. P. Perdew, K. Burke, M. Ernzerhof, *Phys. Rev. Lett.* **1997**, *78*, 1396–1399; c) C. Adamo, V. Barone, *J. Chem. Phys.* **1999**, *110*, 6158–6170.

[38] a) P. J. Hay, W. R. Wadt, *J. Chem. Phys.* **1985**, *82*, 270–283; b) W. R. Wadt, P. J. Hay, *J. Chem. Phys.* **1985**, *82*, 284–298; c) P. J. Hay, W. R. Wadt, *J. Chem. Phys.* **1985**, *82*, 299–310.

[39] P. C. Hariharan, J. A. Pople, *Mol. Phys.* **1974**, *27*, 209–214.

[40] a) C. Jamorski, M. E. Casida, D. R. Salahub, *J. Chem. Phys.* **1996**, *104*, 5134–5147; b) M. Petersilka, U. J. Grossmann, E. K. U. Gross, *Phys. Rev. Lett.* **1996**, *76*, 1212–1215; c) R. Bauernschmitt, R. Ahlrichs, F. H. Hennrich, M. M. Kappes, *J. Am. Chem. Soc.* **1998**, *120*, 5052–5059; d) M. E. Casida, *J. Chem. Phys.* **1998**, *108*, 4439–4449; e) R. E. Stratmann, G. E. Scuseria, M. J. Frisch, *J. Chem. Phys.* **1998**, *109*, 8218–8224.

[41] M. T. Cancès, B. Mennucci, J. Tomasi, *J. Chem. Phys.* **1997**, *107*, 3032–3041.

[42] Gaussian 03, Revision C.02, M. J. Frisch, G. W. Trucks, H. B. Schlegel, G. E. Scuseria, M. A. Robb, J. R. Cheeseman, J. A. Montgomery, Jr., T. Vreven, K. N. Kudin, J. C. Burant, J. M. Millam, S. S. Iyengar, J. Tomasi, V. Barone, B. Mennucci, M. Cossi, G. Scalmani, N. Rega, G. A. Petersson, H. Nakatsuji, M. Hada, M. Ehara, K. Toyota, R. Fukuda, J. Hasegawa, M. Ishida, T. Nakajima, Y. Honda, O. Kitao, H. Nakai, M. Klene, X. Li, J. E. Knox, H. P. Hratchian, J. B. Cross, V. Bakken, C. Adamo, J. Jaramillo, R. Gomperts, R. E. Stratmann, O. Yazyev, A. J. Austin, R. Cammi, C. Pomelli, J. W. Ochterski, P. Y. Ayala, K. Morokuma, G. A. Voth, P. Salvador, J. J. Dannenberg, V. G. Zakrzewski, S. Dapprich, A. D. Daniels, M. C. Strain, O. Farkas, D. K. Malick, A. D. Rabuck, K. Raghavachari, J. B. Foresman, J. V. Ortiz, Q. Cui, A. G. Baboul, S. Clifford, J. Cioslowski, B. B. Stefanov, G. Liu, A. Liashenko, P. Piskorz, I. Komaromi, R. L. Martin, D. J. Fox, T. Keith, M. A. Al-Laham, C. Y. Peng, A. Nanayakkara, M. Challacombe, P. M. W. Gill, B. Johnson, W. Chen, M. W. Wong, C. Gonzalez, J. A. Pople, Gaussian, Inc., Wallingford CT, **2004**.

[43] a) AOMix: Program for Molecular Orbital Analysis, S. I. Gorelsky, http://www.sg-chem.net/, University of Ottawa (Canada), **2007**; b) S. I. Gorelsky, A. B. P. Lever, *J. Organomet. Chem.* **2001**, *635*, 187–196.

Received: October 21, 2009
Published online: March 12, 2010

